Synthesis of Water Dispersible and Catalytically Active Gold-decorated Cobalt Ferrite Nanoparticles

Alessandro Silvestri[†‡], *Sara Mondini*[†‡], *Marcello Marelli*[†], *Valentina Pifferi*[‡], *Luigi Falciola*[‡], *Alessandro Ponti*[†], *Anna M. Ferretti*[*†] *and Laura Polito*[*†]

† Laboratorio di Nanotecnologie, Istituto di Scienze e Tecnologie Molecolari, Consiglio Nazionale delle Ricerche, Via G. Fantoli 16/15, 20138 Milan, Italy

‡ Department of Chemistry, University of Milan, Via C. Golgi 19, 20133 Milan, Italy

ABSTRACT. Hetero-nanoparticles represent an important family of composite nanomaterials that, in the last years, is attracting ever growing interest. Here, we report a new strategy for the synthesis of water dispersible cobalt ferrite nanoparticles ($Co_xFe_{3-x}O_4$ NPs) decorated with ultrasmall (2-3 nm) gold nanoparticles (Au NPs). The synthetic procedure is based on the use of 2,3-*meso*-dimercapto succinic acid (DMSA), which plays a double role. Firstly, it transfers cobalt ferrite NPs from the organic phase to aqueous media. Secondly, the DMSA reductive power promotes the *in-situ* nucleation of gold NPs in proximity of the magnetic NP surface. Following this procedure, we achieved a water dispersible nano-system ($Co_xFe_{3-x}O_4$-DMSA-Au NPs) which combines the cobalt ferrite magnetic properties with the catalytic features of ultrasmall Au NPs. We showed that $Co_xFe_{3-x}O_4$-DMSA-Au NPs act as an efficient nano-catalyst to reduce 4-nitrophenol to 4-aminophenol, and that they can be magnetically recovered and

recycled. It is noteworthy that such nanosystem is more catalytically active than Au NPs with equal size. Finally, a complete structural and chemical characterization of the hetero-NPs is provided.

1. INTRODUCTION

One of the most compelling goals in the field of nanotechnology is the design and synthesis of hetero-nanoparticles, combining in a single entity the physical and chemical properties of the composing substances.[1-5] In addition to this additive multi-functionality, hybrid nanostructures can synergistically enhance the capabilities of the individual component due to proximity effects or electronic coupling at the interface.[6] By engineering at the nanoscale, it is possible to design and create new materials with improved and fascinating properties, which can be employed in many applications.[1-5] Among a wide number of papers related to the production of hybrid nano-structures,[1-7] a large focus has been placed on the synthesis of hybrid magnetic nanoparticles (NPs), mainly based on magnetite/maghemite (Fe_3O_4/γ-Fe_2O_3) and gold.[8] These materials have been extensively studied and synthesized with different types of morphologies like core-shell,[9-11] inverted core-shell,[12] and dumbbell.[13-15] The reason for this huge interest resides in the large number of applications in which gold-coated magnetic NPs can be used. In fact, tailoring their features, these materials can be applied in the fields of nanomedicine,[7,16] biosensors,[16,17] cell separation[16,17] and catalysis.[18,19] The optical and catalytic activity of gold can be modulated by sizing and shaping the Au NP morphology or the hetero-nanoparticle geometry. For example, the plasmon resonance peak of Au could be shifted to the NIR region by increasing size or introducing branches on the NP surface.[20] Furthermore an increase in the surface/volume ratio plays a fundamental role in the catalytic activity of nanometric gold.[21,22] On the other hand,

magnetic properties can be fine tuned controlling the size and composition of ferrite NPs. For instance, in comparison with magnetite/maghemite (Fe_3O_4/γ-Fe_2O_3), cobalt ferrite ($CoFe_2O_4$) NPs present improved magnetic properties due to their high relaxivity and magnetic anisotropy.[23,24] Despite advantageous magnetic properties, few examples of hybrid systems comprising cobalt ferrites and gold have been described.[25-28] Moreover, an inherent difficulty in the reproducible synthesis of these hetero-nanoparticles hamper their widespread exploitation.[2] Herein, we report a reliable synthetic strategy to obtain water dispersible cobalt ferrite NPs decorated with ultrasmall gold NPs ($Co_xFe_{3-x}O_4$-DMSA-Au), by means of a facile protocol. The multistep strategy is based on the solvothermal synthesis of cobalt ferrite nanoparticles, stabilized by oleic acid and oleylamine ($Co_xFe_{3-x}O_4$-OA) in organic solvent, followed by a ligand exchange procedure to bring the NPs in aqueous environment, by using 2,3-*meso*-dimercapto succinic acid ($Co_xFe_{3-x}O_4$-DMSA). Next, the DMSA coating the magnetic NP surface was exploited to reduce $AuCl_4^-$ and to induce an *in situ* nucleation of gold NPs exclusively in the proximity of the cobalt ferrite surface, without using any further reducing agents or preformed gold seeds. The presence of a wide available surface area of noble metal onto a nanosized magnetic support, makes this material a promising candidate to act as an efficient recyclable catalyst. Therefore, taking advantage of their water solubility and magnetization, we studied the catalytic reduction of 4-nitrophenol (4-NP) to 4-aminophenol (4-AP), monitoring the reaction progress by UV-vis spectroscopy. The chance to reduce, at room temperature and in mild conditions, water pollutants is presently of crucial interest.[29,30] Nitroaromatics, in fact, are an important class of environmentally toxic compounds widely employed in the production of explosives, pesticides, plastics and pharmaceuticals.[29] Noteworthy, the molecule resulting from this reduction (4-AP) can find applications in many fields, underlying the opportunity to carry on

new studies to continuously improve the reduction efficiency.[29,30] The morphological, elemental and structural features of hetero-nanoparticles were evaluated by Transmission Electron Microscopy (TEM), Inductively Coupled Plasma-Optical Emission Spectrometers (ICP-OES), UV-Vis spectroscopy and Dynamic Light Scattering (DLS) analysis.

2. EXPERIMENTAL SECTION

2.1 Materials. All reagents, unless cited otherwise, were purchased from Sigma-Aldrich, and used without any further purification. $HAuCl_4 \bullet 3H_2O$ was stored as a 10 mM solution in MilliQ water, at 4 °C and protected from light. The glassware used for gold NPs synthesis were cleaned with *aqua regia* (HCl (37%) / HNO_3 (65%) 3/1). Ultra-pure MilliQ water was used for the preparation of all the aqueous solutions. The concentration of water dispersible NPs was performed by means of Millipore Amicon® Ultra centrifugal filters with a 30 kDa cut-off for $Co_xFe_{3-x}O_4$-DMSA NPs and $Co_xFe_{3-x}O_4$-DMSA-Au NPs, and with a cut-off of 3 kDa for Au-DMSA NPs. The purification of NPs was performed by using dialysis tubes with a cut-off of 14 kDa. The dropped addition of $HAuCl_4$ to the reaction mixture was performed with the aid of a NE-1010 Higher Pressure Programmable Single Syringe Pump.

2.2. Synthesis of $Co_xFe_{3-x}O_4$-OA NPs. $Co_xFe_{3-x}O_4$-OA NPs were synthesized according to a literature procedure.[31] A solution of $Fe(acac)_3$ (350 mg, 0.99 mmol), $Co(acac)_2$ (128 mg, 0.495 mmol), oleic acid (1 mL, 3.15 mmol), oleylamine (1 mL, 3.04 mmol), 1,2- hexadecanediol (1.15 g, 4.45 mmol) in benzyl ether (25 mL) was warmed up to 120 °C under argon flow and kept at this temperature for 1 h. The mixture was first heated to 210 °C with a rate of 8 °C/min and maintained at this temperature for 2 h. Then, the temperature was raised to 300 °C with a rate of 3 °C/min and maintained for 1 h. After cooling the reaction mixture to room temperature, the

obtained NPs were collected by centrifugation (6000 rpm) after the addition of a mixture of ethanol/acetone 1/1 and then redissolved in hexane. This treatment was repeated two times. After the last precipitation, $Co_xFe_{3-x}O_4$-OA NPs were stored dissolved in hexane (20 mL) and stored at room temperature.

2.3. Synthesis of water dispersible $Co_xFe_{3-x}O_4$-DMSA NPs. The ligand exchange procedure leading to the title product was performed in two steps. In the first step, 3 mL of hexane solution of $Co_xFe_{3-x}O_4$-OA were precipitated by centrifugation (after adding 10 mL of ethanol/acetone 1/1 mixture) and redissolved in 6 mL of toluene. A solution of DMSA (33 mg, 0.18 mmol) in DMSO (2 mL) were dropped into a round-bottom flask (immersed in a ultrasonic bath) containing the toluene dispersion of $Co_xFe_{3-x}O_4$-OA NPs. The mixture was sonicated for 1 h and further magnetically stirred for 2 days. Afterwards, 4 mL of toluene were added to aid the precipitation of the $Co_xFe_{3-x}O_4$-DMSA NPs. The NPs were magnetically recovered and washed consecutively three times with ethanol and two times with acetone, and finally suspended in MilliQ water (10 mL). Then, to improve aqueous dispersion, the solution was basified to pH 10 (using aq. NaOH solution, 0.1 M) and subsequently brought back to pH 7 (using aq. HCl solution, 0.1 M).[26] In the second step, a solution of DMSA (20 mg, 0.1 mmol) in water (10 mL) was added dropwise to the NP dispersion, and the mixture was sonicated for 1 h. Then the mixture was magnetically stirred for further 12 h and purified by dialyzing against MilliQ water for 72 h (changing water every 8-10 h). Finally, the recovered $Co_xFe_{3-x}O_4$-DMSA NPs were stored as diluted aqueous solution (250 mL), with an iron concentration of 34 μg/mL. Such stock solution was stable for months at room temperature.

2.4. Synthesis of $Co_xFe_{3-x}O_4$-DMSA-Au NPs. In a round-bottom flask, 10 mL of the stock solution of $Co_xFe_{3-x}O_4$-DMSA NPs were stirred (750 rpm) under N_2 atmosphere at room

temperature. An aqueous solution of $HAuCl_4$ (10 mL, 0.2 mM) was slowly dropped into the reaction mixture with the aid of a syringe pump (flow rate: 41.5 μL/min). After completing the addition, the mixture was stirred for an additional hour. The NPs were concentrated, dialyzed against MilliQ water for 48 h (changing water every 8-10 h) and stored as aqueous dispersion (2 mL) with an iron concentration of 140 μg/mL (2.51 mM) and a gold concentration of 86 μg/ml (0.44 mM).

2.5. Synthesis of Au-DMSA NPs. Au-DMSA NPs were synthesized following the method published by Negishi et al.[32] DMSA (1.8 mg, 10 μmol) was dissolved in MilliQ water (0.5 mL) and added to an aqueous solution (5 mL) of $HAuCl_4$ (1.7 mg, 5 μmol). The reaction mixture was stirred (750 rpm) for 10 min at room temperature, and the color of the solution changed from yellow to light brown. The NPs were washed five times with MilliQ water by centrifugation, using 3 kDa centrifugal filters units. The recovered Au-DMSA NPs were dissolved and stored in aqueous solution (4 mL) at a gold concentration of 240 μg/mL.

2.6. Characterization of NPs. The morphology and size distribution of the NPs were evaluated using transmission electron microscopy by means of a Zeiss LIBRA 200FE microscope, equipped with a 200 kV FEG an in-column second-generation omega filter for energy selective spectroscopy, and a STEM facility with HAADF detector. Both TEM and STEM imaging modes were employed. Electron energy loss spectroscopy (EELS) and imaging (ESI), and energy dispersive X-ray spectroscopy (EDX) (OXFORD X-Stream 2 and INCA software) were used to determine the elemental ratio and distribution inside the nanostructure. The samples for TEM analysis were prepared depositing a drop of NP dispersion on a carbon-coated copper grid (300 mesh) and evaporating the solvent. The particle size distribution was obtained by measuring at least 500 nanoparticles, analyzing TEM images by the software Pebbles and Pebble Juggler.[33]

UV-Vis spectra were recorded by means of an Agilent 8453 instrument. DLS and ζ-potential measurements were carried out by a 90 plus Particle Size Analyzer (Brookhaven Instrument Corporation) equipped with a solid state He–Ne laser (wavelength = 661 nm). Experiments were carried out at a scattering angle of 90° on diluted NP samples at 298 K. NP samples for DLS were filtered through 0.45 μm cellulose acetate syringe filters before measuring. Each sample was allowed to equilibrate for 3 min prior to starting the experiment. Ten independent measurements of 60 s duration were performed for each sample. The NP hydrodynamic diameters were calculated using Mie theory, considering absolute viscosity and refractive index values of the medium to be 0.911 cP and 1.334, respectively. The ζ-potential was calculated from the NP electrophoretic mobility using the Smoluchowski theory, assuming a medium viscosity of 0.891 cP, medium dielectric constant of 78.6, and Henry function of 1.5. FTIR spectra were recorded by a Thermo Nicolet NEXUS 670 FTIR spectrometer, using KBr pellets. Gold, iron and cobalt content of NPs was determined *via* Inductively Coupled Plasma-Optical Emission Spectrometry (ICP-OES; iCAP 6300 Duo, Thermofisher). Samples were heated and acid digested with *aqua regia* (500 μL for 5 times); the residues were recovered with HCl 37% (500 μL) and diluted with MilliQ water to a known volume. Multi-element standards containing the three metals were used to create the external calibration line. The magnetic characterization was performed by a Quantum Design MPMS XL-5 SQUID magnetometer. Weighted amounts of powdered samples were packed in Teflon ribbon. The temperature dependence of the magnetization was recorded in the temperature range T = 5 – 300 K using a measuring field H_{meas} = 10 Oe in both zero-field cooling (ZFC) and FC (H_{cool} = 10 Oe) modes. Magnetization isotherms (hysteresis loops) were measured between +50 and –50 kOe at T = 5 K after cooling in zero field. All data were corrected for diamagnetic contributions.

2.7. Catalytic reduction of 4-nitrophenol. The reaction was performed in a 3 mL quartz cell, equipped with a magnetic stirrer and a cap. $Co_xFe_{3-x}O_4$-DMSA-Au NPs ([Au]=0.44 mM) were added to a solution of 4-nitrophenol (1.83 mL, 0.1 mM) in different mole percentages with respect to the substrate (44, 22 or 9 μL of NP dispersion, corresponding to 10, 5 and 2% Au:substrate molar ratio, respectively). Then, an aqueous solution of $NaBH_4$ (330 μL, 500 mM) was added to the mixture (initial reaction time). The transformation ratio was followed monitoring the absorption at 400 nm and 550 nm (see SI) of the reaction mixture at intervals of 1 minute. After each catalytic cycle, the NP catalyst was magnetically recovered by removal of the supernatant. The collected NPs were washed with water and fresh 4-nitrophenol and $NaBH_4$ solutions were introduced in the cell to start a new catalytic cycle. For the control reactions, the same procedure described above for the 10% molar ratio case was carried out, using $Co_xFe_{3-x}O_4$-DMSA NPs (180 μL, [Fe]=0.6 mM) and Au-DMSA NPs (14 μL, [Au]=1.2 mM, 10% molar ratio) as catalyst.

2.8 Electrochemical reduction of 4-nitrophenol. Electrochemical investigations were performed using an Autolab PG-Stat 12 (Ecochemie, The Netherlands) potentiostat/galvanostat, in a conventional three electrodes cell with a saturated calomel reference electrode and a platinum wire counter electrode. The working electrode was a glassy carbon one (AMEL, Italy, 3 mm diameter), modified by drop casting with a Kartell micropipette 20 μL of a solution of the nanomaterials: $Co_xFe_{3-x}O_4$-DMSA-Au NPs ([Au]=0.44 mM), $Co_xFe_{3-x}O_4$-DMSA NPs ([Fe]=0.6 mM), Au-DMSA NPs ([Au]=0.4 mM). Current densities were determined dividing the experimental currents by the electrode geometric area. Prior to modification, the GC support electrode surface was cleaned with synthetic diamond powder (Aldrich, diameter 1 μm, 99.9%) on a Struers DP Nap wet cloth and rinsed in water. 0.1 M $NaClO_4$ (Sigma Aldrich) was used as

supporting electrolyte in aqueous media (20 mL) and mixed with a saturated solution of 4-nitrophenol (60 µL).

3. RESULTS AND DISCUSSION

3.1. Synthesis of water dispersible cobalt ferrite. To produce hetero-NPs we tuned a multi-step protocol (Scheme 1).

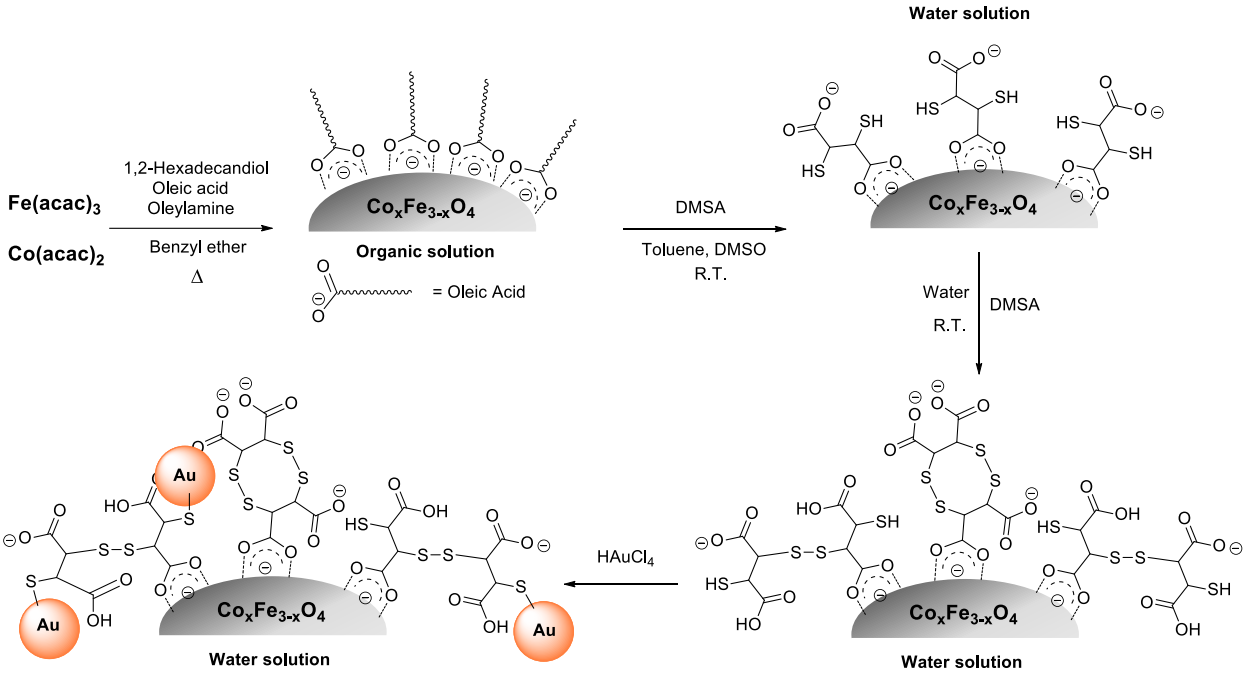

Scheme 1. Synthetic strategy for $Co_xFe_{3-x}O_4$-DMSA-Au NPs.

The initial step consisted in the synthesis of organic dispersible cobalt ferrite ($Co_xFe_{3-x}O_4$-OA NPs), fabricated according to the procedure published by Zhu et al.[31] by means of the solvothermal decomposition of iron(III) and cobalt(II) acetylacetonate precursors. This procedure allowed us to have an efficient control over the morphology of superparamagnetic NPs synthesis. We slightly modified the literature protocol by employing 1,2-hexadecanediol as

a mild reducing agent, that guarantees the monocrystallinity of cobalt ferrite nanocrystals.[34] The obtained NPs had spheroidal shape (median equivalent diameter = 7.8 ± 1.2 nm, Figure 1a and Figure S1) and both the electron diffraction pattern and the HRTEM fringes (Figure S2) correspond to a cubic ferrite.

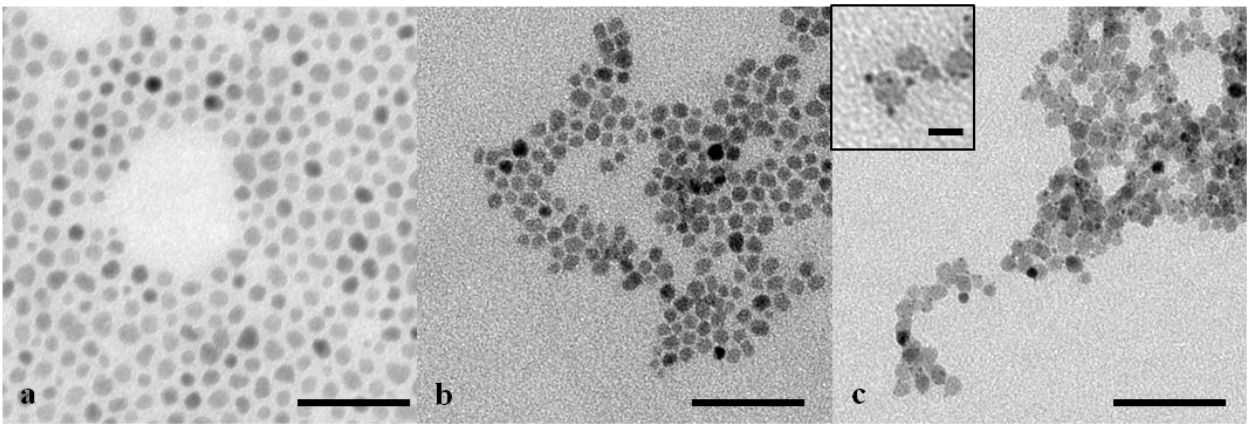

Figure 1. TEM images (scale bar = 50 nm) of a) $Co_xFe_{3-x}O_4$-OA NPs, b) $Co_xFe_{3-x}O_4$-DMSA NPs and c) $Co_xFe_{3-x}O_4$-DMSA-Au NPs with an expansion in the inset (bar 10 nm).

The chemical composition of the NPs has been investigated by recording EELS spectra (Figure 2a) on a grid area of about 0.36 μm^2. In the spectra the Fe-$L_{2,3}$ edge (beginning at 708 eV) and the Co-$L_{2,3}$ edge (beginning at 779 eV) can be observed. To calculate the molar ratio between Fe and Co we fitted the spectra using the best-fit procedure implemented in the EELS Model 3.3 software,[35] obtaining an atomic Fe:Co ratio equal to 2.7±0.9 (x=0.8±0.2). By the ESI maps (Figure 2c,d), which provide an image of the distribution of a specific element, it is evident that both metal ions are present in each NPs. Thus, we established that the two metals were homogeneously distributed in the sample. This finding, along with the diffraction data, showed that we truly obtained cobalt ferrite NPs and not a mixture of iron oxide NPs and cobalt oxide NPs. Moreover, using the independent spectroscopic technique EDX (figure S3), we measured

the atomic percentage of Fe = 69.8% and Co = 30.2% that correspond to an atomic Fe:Co ratio of 2.31 (x = 0.91). This experiment was performed on a grid area of about 2.5 μm^2, larger than that sampled in the EELS experiment. The Fe:Co ratio obtained by EELS and EDX are in a good agreement and show the quasi stoichiometric composition of the cobalt ferrite NPs with x ≅ 0.9.

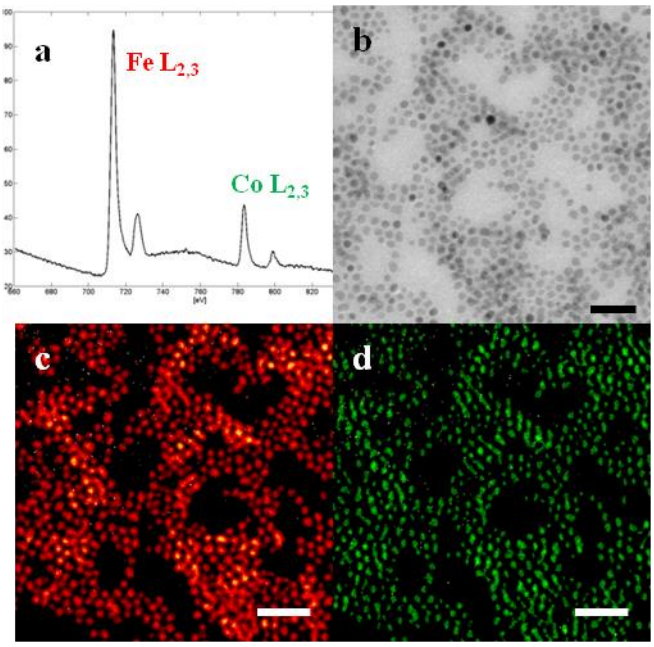

Figure 2. a) EELS spectrum of $Co_xFe_{3-x}O_4$-OA NPs where the two edges starting at 708eV and 779eV, correspond to the $FeL_{2,3}$ and $CoL_{2,3}$ edges, respectively; b) Reference TEM image to be compared with the ESI maps of iron (c, red) and cobalt (d, green). The bars correspond to 50 nm.

The second step was focused on the exchange of surfactants, to remove the long-chain hydrophobic ligands (oleic acid, oleylamine) which coated the metal oxides NPs and to bring them in water media. To accomplish the exchange, we chose to use 2,3-*meso*-dimercaptosuccinic acid (DMSA), a ligand well known in literature for its ability to transfer ferrite NPs from organic to aqueous media.[36] The literature procedure was improved by adding a second exchange step. First, a solution of DMSA in DMSO was dropped into a toluene dispersion of $Co_xFe_{3-x}O_4$-OA

NPs. The substitution of OA with DMSA lets NPs to precipitate in toluene and then to be dispersed in water. During the second step, the aqueous NP dispersion was treated with an excess of DMSA, in order to improve its colloidal stability in water (Figure 1b and Figure S4-6). NPs treated with an excess of DMSA resulted in a decreased aggregation on the TEM grid (Figure S5), confirmed by the size distributions obtained by DLS (Figure S7). Figure S7, in fact, show a decreased hydrodynamic size and distribution from the first to the second step of the ligand exchange procedure, underlining the improvement in stability and dispersion. To evaluate the colloidal stability before and after the treatment with the excess of DMSA, we measured the variation of ζ-potential of NP solution, as a function of pH and ionic strength of the medium.[37-39] At a fixed ionic strength ([KCl]=1 mM), the pH of the NP dispersion was tuned in a range between 2 and 12 by adding aq. NaOH or aq. HCl (0.5 M) (Figure S8a), registering that the NP dispersion, obtained after the second addition of DMSA, had a slight increment of negative ζ-potential and thus an improved colloidal stability at pH > 3.5.[37,39] At pH < 3.5, $Co_xFe_{3-x}O_4$-DMSA NPs treated with the excess of DMSA displayed a rapid increase of ζ-potential that could be ascribed to the protonation of free carboxylic groups of DMSA (pK_1 2.71, pK_2 3.48). The influence of the ionic strength on the $Co_xFe_{3-x}O_4$-DMSA NPs colloidal stability was evaluated increasing the concentration of KCl in a phosphate-buffered NP dispersion (PBS, pH=7). The data (Figure S8b) showed lower ζ-potential values for higher ionic strengths,[38] as expected for charged NPs, and confirmed the improved stability of NPs obtained after the treatment with the excess of DMSA in a large range of ionic force. FT-IR spectra (Figure S9) are in agreement with the literature data,[39] confirming the success of the ligand exchange procedure. By means of ICP-OES measurements (Figure S10), the atomic Fe:Co ratio in $Co_xFe_{3-x}O_4$-DMSA NPs was established to be 71:29 (x = 0.87), confirming the result obtaining by EELS and EDX

experiments on $Co_xFe_{3-x}O_4$-OA NPs. Therefore, the "two-steps" ligand exchange procedure did not alter the chemical composition of the ferrite NPs.

3.2. Synthesis of gold decorated cobalt ferrite. The obtained water dispersible $Co_xFe_{3-x}O_4$-DMSA NPs were used as a substratum for the localized growth of ultrasmall gold NPs, exploiting the known reducing ability of DMSA for the production of nanometer sized gold nanoparticles.[32] Recently, Carlà et al.[26] described the production of core-shell $CoFe_2O_4$/Au composites, by using DMSA as stabilizing agent for $CoFe_2O_4$ NPs and a sonochemical process to achieve the reduction of gold salts. In another paper, Odio et al.[40] took advantages of the ability of magnetite-DMSA NPs to adsorb gold ions from aqueous environments, recording the formation of reduced gold. Drawing inspiration from literature, we exploited the double role that DMSA can play to produce controlled and water dispersible cobalt ferrite/gold hetero-structured NPs (Scheme 1), by slowly dropping $HAuCl_4$ in a $Co_xFe_{3-x}O_4$-DMSA NP solution. In order to optimize the decoration step, we evaluated the influence of two main parameters: the Au^{3+} amount and the rate of its addition. A solution of $HAuCl_4$ (0.2 mM) was dropped (83 µL/min) in 5 mL of $Co_xFe_{3-x}O_4$-DMSA NP water dispersion ([Fe] = 34 µg/mL), supplying three different quantities (10^{-3} mmol, $2\cdot10^{-3}$ mmol, $4\cdot10^{-3}$ mmol). The addition of 10^{-3} mmol of Au^{3+} resulted in a low decoration level (1.8±1.2 Au NPs/ $Co_xFe_{3-x}O_4$-DMSA NPs) with Au NPs having equivalent diameter < 3 nm (Figure S11a,d). The injection of $4\cdot10^{-3}$ mmol of Au precursor led to a good decoration level (3.1±1.7 Au NPs/ $Co_xFe_{3-x}O_4$-DMSA NPs) but also to the formation of undesired large gold NPs having $d_{equivalent}$>20 nm (Figure S11c,f). The best compromise was achieved using $2\cdot10^{-3}$ mmol of $HAuCl_4$ resulted in 2.4±1.3 Au NPs/ $Co_xFe_{3-x}O_4$-DMSA NPs with Au NPs having equivalent diameter < 3 nm (Figure S10b,e). To evaluate the role of the dropping rate in the decoration step, the optimized quantity of Au^{3+} ($2\cdot10^{-3}$ mmol) was slower added (flow

rate = 41.5 μL/min) or rapid injected. By decreasing the Au^{3+} addition rate, the immediate DMSA/Au ratio in the mixture incremented, promoting the formation of small Au NPs (median diameter 2.7 ± 0.5 nm) with respect to the growth of the larger ones,[41] achieving a decoration of 2.9±1.7 Au NPs per $Co_xFe_{3-x}O_4$-DMSA NP (Figure 4, S11g and S13-14). While, the sample obtained by the single injection present a low decoration degree (1.4±1.7 Au NPs per $Co_xFe_{3-x}O_4$-DMSA NP) and the presence of larger Au NPs with d_{median}=28 ± 8 nm (Figure 4c and Figure S12).[41] Moreover, comparing UV-vis spectra (Figure 3a), the surface plasmonic resonance (SPR) peak at 550 nm, correlated to the presence of large Au NPs, is evident only in the sample obtained by single injection.[20,42] SPR peak is barely visible in the $Co_xFe_{3-x}O_4$-DMSA-Au NP solution obtained by the dropped addiction, confirming the scarce presence of large Au NPs.

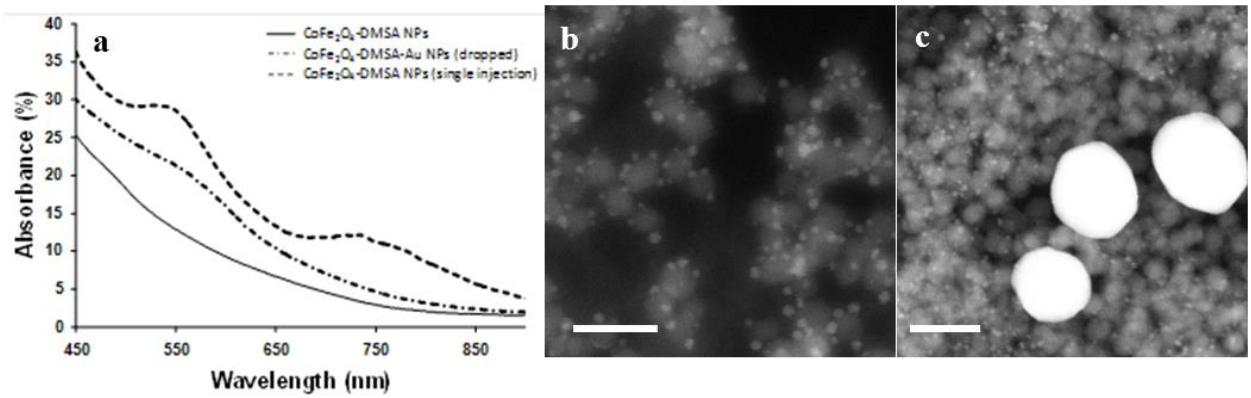

Figure 3. a) UV-Vis spectra of the $Co_xFe_{3-x}O_4$-DMSA NPs and $Co_xFe_{3-x}O_4$-DMSA-Au NPs obtained by a single injection or by a slow dropping (41.5 μL/min); b) STEM Image of $Co_xFe_{3-x}O_4$-DMSA-Au NPs obtained by slow dropping; c) STEM Image of $Co_xFe_{3-x}O_4$-DMSA-Au NPs obtained by single injection. The scale bars correspond to 20 nm.

TEM and STEM images confirmed the information obtained from UV-vis spectra (Figure 1c and Figure 3b,c). STEM images show the high degree and uniformity of decoration that can be obtained following the optimized synthetic strategy (Figure 3b and Figure S15). As expected, we identified in the electron diffraction of the $Co_xFe_{3-x}O_4$-DMSA-Au NPs (Figure S16) the two

patterns corresponding to Au and $Co_xFe_{3-x}O_4$. The atomic ratio between Fe, Co and Au was quantified by ICP-OES measurement as Fe:Co:Au = 72:13:14. After gold decoration, a variation in the ratio between Fe and Co was detected, corresponding to a decrease in cobalt content[26] ($x \cong 0.5$) (Figure S17). This result is in agreement with the elemental composition measured using EDX spectroscopy (Figure S18). In summary, the best synthetic outcome – extensive decoration and minimization of the presence of large gold NPs – is achieved by slow injection (flow rate = 41.5 µL/min) of 0.33 eq of gold precursor, calculated with respect to the iron content of the ferrite NPs.

3.3. Magnetic properties of cobalt ferrite NPs.

We investigated the magnetic properties of the cobalt ferrite nanocrystals before and after the gold decoration in order to study the effects of the decrease of the cobalt content (Figure 4 and Figure S19-S20). The main magnetic parameters are reported in Table 1.

Table 1. Magnetic parameters of $Co_xFe_{3-x}O_4$-DMSA and $Co_xFe_{3-x}O_4$-DMSA-Au NPs

Sample	H_c (kOe)	M_s (emu/g)	M_r (emu/g)	M_s/M_r	T_{max} (K)	T_{der} (K)
$Co_xFe_{3-x}O_4$ DMSA	14.9	142	113	0.79	240	200
$Co_xFe_{3-x}O_4$ DMSA-Au	14.5	107	84	0.78	270	230

The isothermal magnetization $M(H)$ of both samples presents a broad hysteresis loop with large coercive field typical of magnetically hard cobalt ferrite (Figure 4). The coercive field H_c of both samples is typical of cobalt ferrite NPs and smaller than the bulk value of 25.2 kOe.[43] H_c is only slightly smaller after gold decoration despite the substantial Co loss (x decreases from 0.87 to 0.46). It was however recently observed[44] that in sub-stoichiometric $Co_xFe_{3-x}O_4$ NPs the magnetic properties quickly change when x is small and level off about $x = 0.5$, in accordance with the present observation. The recorded hysteresis loops are almost, but not exactly, major loops and the saturation magnetization M_S values might therefore be slightly underestimated. M_S

decreases from 142 to 107 emu/g upon gold decoration. Both values are larger than the M_S bulk value, (93 emu/g at 5K).[43]

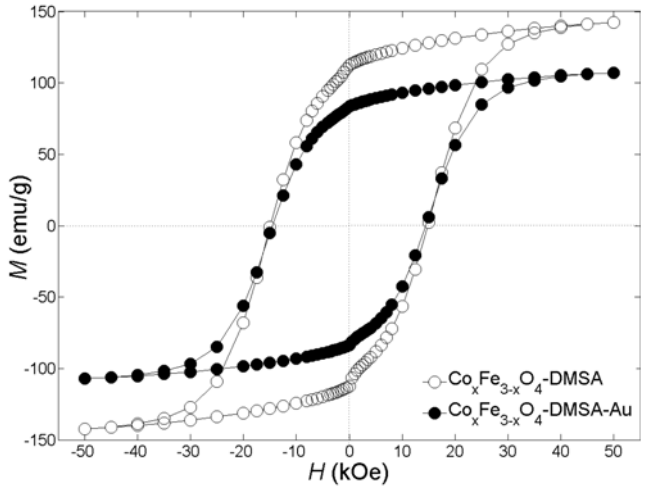

Figure 4. Hysteresis loops of the cobalt ferrite samples before and after gold decoration. Hollow circles: $Co_xFe_{3-x}O_4$-DMSA; solid circles: $Co_xFe_{3-x}O_4$-DMSA-Au.The magnetization is given relative to the mass of cobalt ferrite.

Such large values are difficult to interpret since electron diffraction excluded the presence of non-ferritic phases with larger magnetization. A similar effect has been observed in small (3 nm) stoichiometric cobalt ferrite NPs diluted in a silica matrix and ascribed to frozen canted spins located in a 0.3 nm thick surface shell of the ferrite nanocrystal.[45] However, it is uncertain if this conclusion can also be drawn for our 7.8 nm sub-stoichiometric undiluted cobalt ferrite nanocrystals. The squareness ratio M_r/M_s is 0.79 and 0.78 for $Co_xFe_{3-x}O_4$ DMSA and $Co_xFe_{3-x}O_4$ DMSA-Au respectively, close to the value predicted for non-interacting randomly-oriented Stoner-Wohlfahrt nanocrystals having cubic magnetocrystalline anisotropy.[46,47] Such high values have already been observed in nanocomposites containing cobalt-ferrite NPs in a polyaniline matrix.[48] We also measured the zero field cooling (ZFC) and field cooling (FC) magnetization curves of both samples as a function of the temperature (from 5 to 300 K) using a measuring field of 10 Oe (Figure S19-S20). These curves are typical of magnetic nanoparticles and clearly display the transition to the superparamagnetic regime at high temperature. In general, the

behavior of both samples agrees with the prediction that cobalt ferrite nanoparticles having diameter < 10 nm are superparamagnetic at 300 K.[49] Several proposal have been made to estimate the average blocking temperature from ZFC/FC curves. A popular choice is the temperature T_{max} where M_{ZFC} reaches its maximum value. We observed T_{max} = 240 and 270 K in the case of $Co_xFe_{3-x}O_4$ DMSA and $Co_xFe_{3-x}O_4$ DMSA Au NPs, respectively. The latter value is in agreement with a literature value for ferrite NPs with similar cobalt content.[44] A deeper insight into the blocking/unblocking behavior of the NPs can be achieved by computing the derivative $-d(M_{FC} - M_{ZFC})/dT$, which is an approximate representation of the distribution of the magnetic anisotropy energy barriers (Figure S19-S20).[50] The most probable barrier is at T_{der} = 200 and 230 K for $Co_xFe_{3-x}O_4$-DMSA and $Co_xFe_{3-x}O_4$-DMSA-Au NPs, respectively. Both estimates thus indicate that the blocking temperature increases by about 30 K upon loss of cobalt caused by the gold decoration. This is unexpected since (i) the cobalt ferrite size does not significantly change upon gold decoration and (ii) cobalt ions largely add to the global magnetic anisotropy due to the their strong single-ion anisotropy. At the moment we can only suggest that decoration with gold NPs modifies the interparticle interaction (e.g. the dipole-dipole interaction) in such a way that the cobalt ferrite nanocrystals are subject to a larger global magnetic anisotropy translating into a higher blocking temperature.

3.4. Catalytic application of gold decorated cobalt ferrite. Taking advantage of the magnetic properties of the nanometric ferrite support and the catalytic potential of Au NPs, the produced $Co_xFe_{3-x}O_4$-DMSA-Au NPs could be used as quasi-homogeneous and magnetically recyclable catalyst for red-ox reactions.[19,21,22] In the present study the catalytic activity of optimally-decorated $Co_xFe_{3-x}O_4$-DMSA-Au NPs has been investigated performing the reduction of 4-NP to 4-AP, monitoring the reaction by UV-vis spectroscopy and using $NaBH_4$ as reducing

agent (Figure 5).[29] In the presence of an excess of $NaBH_4$, 4-NP is converted into its sodium salt (4-nitrophenolate) which shows an intense absorption peak at 400 nm. Through monitoring the decreasing of the absorbance at 400 nm during the time, it is possible to follow the kinetics of the reaction (Figure 5).

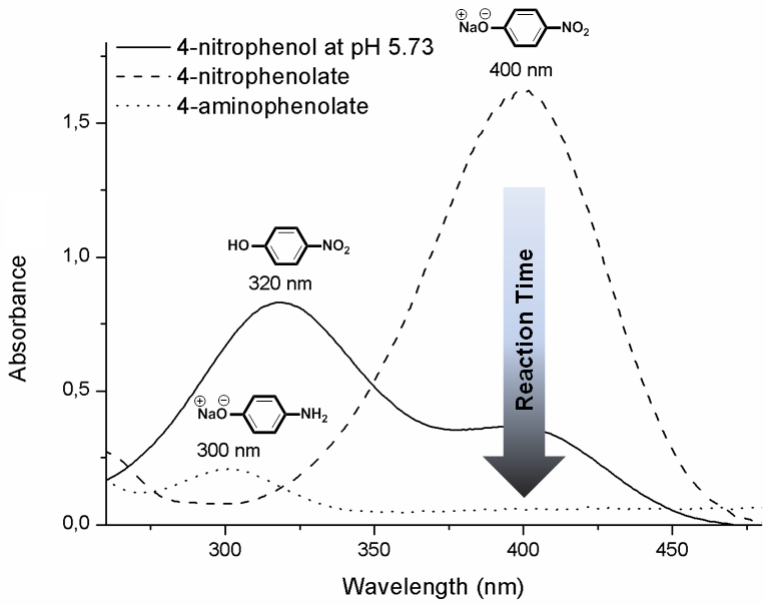

Figure 5. UV-vis spectra of 4-nitrophenol, sodium 4-nitrophenolate and sodium 4-aminophenolate

To evaluate the catalytic efficiency (Figure 6a), three different $Co_xFe_{3-x}O_4$-DMSA-Au NPs amounts have been tested (2, 5 and 10 % molar with respect to Au, as measured by ICP-OES). Furthermore, as negative control, the red-ox reactions were performed without addition of catalyst or by adding the colloidal water solution of cobalt ferrite ($Co_xFe_{3-x}O_4$-DMSA NPs). Either without catalyst or with $Co_xFe_{3-x}O_4$-DMSA NPs, no reaction occurred as expected,[51] indicating that the presence of the noble metal is required for catalysis. Instead, in the presence of $Co_xFe_{3-x}O_4$-DMSA-Au NPs, the reaction was completed in a few minutes after an induction time dependent on the amount of the catalyst. According to the Langmuir–Hinshelwood (LH)[29,52] model (Figure S21) which describes the kinetics of this reaction, both reactants (4-NP and

hydride) need to be adsorbed on the surface of the NPs to react. The observed induction period is then related to the slow restructuring of NP surfaces by the reactants,[52,53] before the reaction starts. To confirm this hypothesis we performed two catalyzed reactions pre-incubating NPs with $NaBH_4$ or with 4-NP: in both cases we still observed an induction time even if shorter (2-4 min vs 6-8 min, Figure S21-S22). The catalytic activity of the hetero-nanoparticles is excellent (Figure 6b and Table S24). For instance, when the catalyst is used at 2% mol (Au), the reaction proceeds with one of the highest rate reported in literature (k_{norm} = 4.4 $\cdot 10^6$ $s^{-1}mol^{-1}$) by using nanosized catalyst.[19] Finally, to compare our catalytic system with a non-magnetically supported one, we synthesized Au-DMSA NPs with a median diameter of 2.1±0.4 nm following a literature procedure (Figure S25a-S26).[32] Using 10% molar of Au-DMSA NPs with respect to 4-NP, the initial activation time was shorter but the reaction rate was drastically slower. In fact, k_{obs} for Au-DMSA NPs was 6 times lower than that observed for the corresponding amount of $Co_xFe_{3-x}O_4$-DMSA-Au NPs (Figure 6b and Table S24).

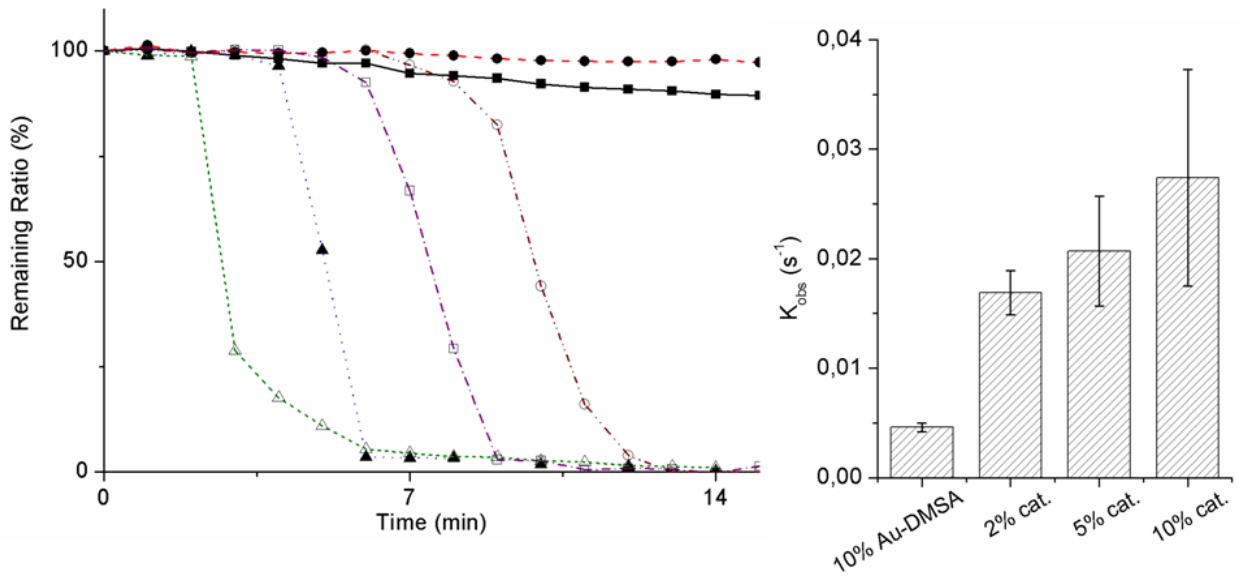

Figure 6. a) The reduction efficiency of 4-NP by: ■ No catalyst; ● $Co_xFe_{3-x}O_4$-DMSA NPs; Δ 10% Au-DMSA NPs; ▲ 10% $Co_xFe_{3-x}O_4$-DMSA-Au NPs; □ 5% $Co_xFe_{3-x}O_4$-DMSA-Au NPs; ○ 2% $Co_xFe_{3-x}O_4$-DMSA-Au NPs. Remaining Ratio is defined as the residual percentage of 4-nitrophenolate in the reaction solution, calculated from the absorbance values as explained in SI. **b)** The observed kinetic constant k_{obs} for 10% Au-DMSA NPs and 2%, 5% and 10% $Co_xFe_{3-x}O_4$-DMSA-Au NPs.

The higher catalytic activity of $Co_xFe_{3-x}O_4$-DMSA-Au NPs respect to Au-DMSA NPs can be ascribed to the unique electronic features of hetero-nanoparticles. Even if the electronic behavior at the metallic interface is still unclear, in literature it is hypothesized that an electron flow from gold to ferrite NPs drives the remarkable improvement in catalytic activity of these kinds of hetero-nanoparticles.[6,54,55] To deeper investigate their catalytic behavior, we carried out an electrochemical reduction of 4-NP. An electrocatalytic effect (100 mV peak shift towards less negative potentials) is observed for all the modified electrodes (Figure 7), testifying the catalytic properties of the investigated materials in the 4-NP reduction reaction. Moreover, in the case of $Co_xFe_{3-x}O_4$ modified electrodes (with or without Au NPs) an increase in peak current densities (i.e. electrochemical reaction rate) is evident, ascribed to an increase of the surface area and thus of the available reactive sites of these materials. This result is in agreement with the previous experiment where k_{obs} calculated for Au-DMSA NPs resulted lower than that observed for $Co_xFe_{3-x}O_4$-DMSA-Au NPs (Figure 6).

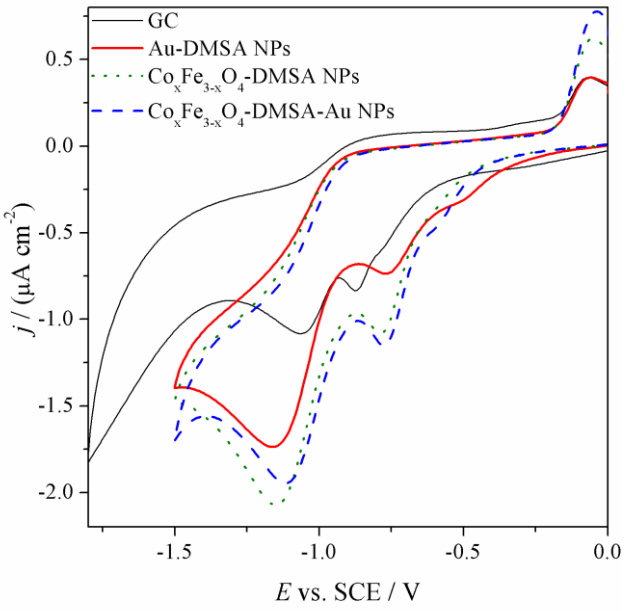

Figure 7. Cyclovoltammetric reduction patterns (0.1 V s^{-1} scan rate) of 4-NP (60 μL of a saturated aqueous solution in 20 ml of 0.1 M $NaClO_4$ aqueous solution) on the GC support and on three different modified electrodes.

Interestingly, from the electrochemical results, it seems that Au NPs does not provide an extra contribute in the direct electrocatalytic reduction of 4-NP, since $Co_xFe_{3-x}O_4$-DMSA NPs can efficiently catalyze the reaction. On the contrary, in our model reaction condition which exploits the use of $NaBH_4$, $Co_xFe_{3-x}O_4$-DMSA NPs are inactive while Au NPs presence is crucial to promote on their surface the absorption and oxidation of sodium borohydride.[56] After this first step, the synergistic effect between Au NPs and cobalt ferrite transfer efficiently the electrons required for the reduction.[52,57] This aspect, together with the increased surface active areas, can explain the best performance registered for $Co_xFe_{3-x}O_4$-DMSA-Au NPs respect to Au-DMSA NPs.

Due to their magnetization, the hybrid NPs can be rapidly (few seconds) and easily recovered using a neodymium-based magnet (Figure S27) and re-dispersed in MilliQ water for further catalytic cycles. To verify the recycling efficiency of the $Co_xFe_{3-x}O_4$-DMSA-Au NPs, we performed 5 consecutive catalytic cycles (Figure 8a). In the first cycle the induction time is not negligible, but it slowly diminishes with the repetition of the cycles, confirming the LH model.[29,52,53]

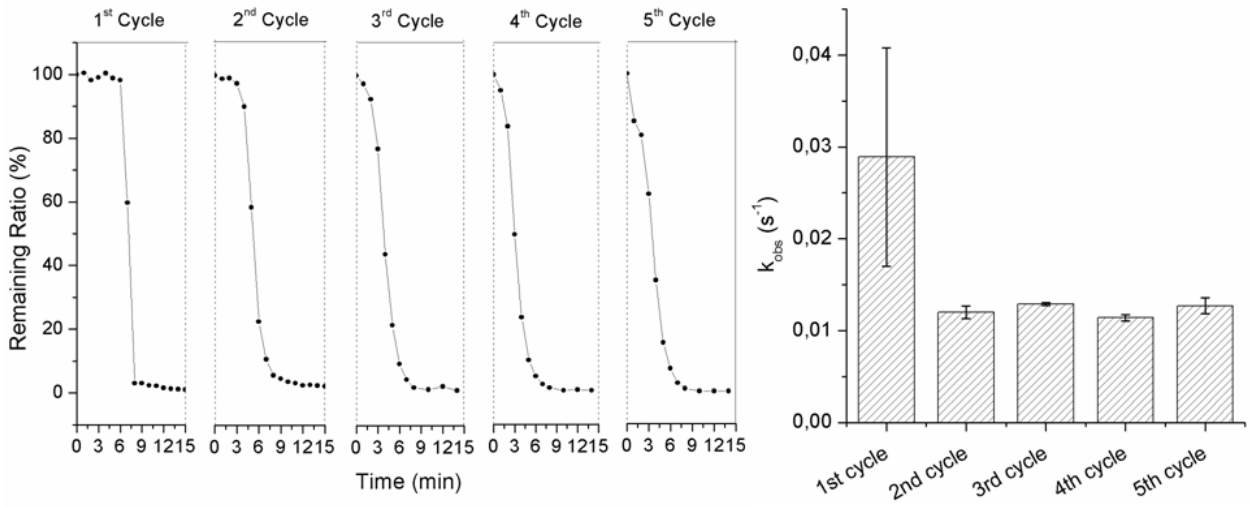

Figure 8. Reduction efficiency of 4-NP in the consecutive catalytic cycles (a) and the corresponding k_{obs} calculated for each cycle (b).

The observed rate constant was calculated for each recycle (Figure 8b). After the first cycle (k_{obs} = $2.7 \cdot 10^{-2}$ s^{-1}), the k_{obs} halved and maintained the value of $1.2 \cdot 10^{-2}$ s^{-1} during the next four cycles. The high performance of the nano-catalyst was also proved by the fact that, even after 5 catalytic cycles, the reduction of 4-NP was complete in less than 10 minutes.

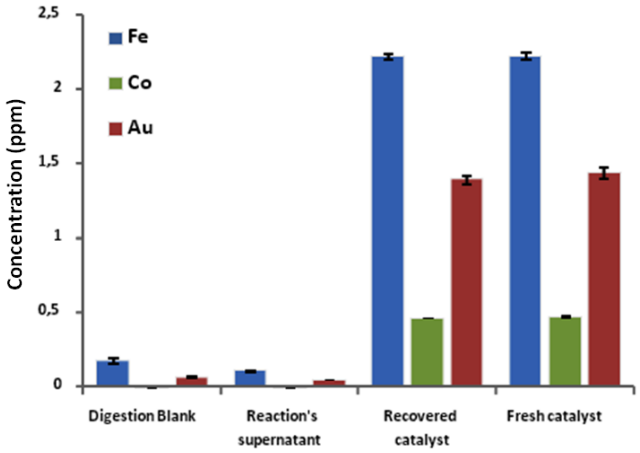

Figure 9. The concentration of Fe, C,o and Au in: digestion blank, catalytic reaction supernatant, recovered catalyst after one catalytic cycle, and fresh catalyst.

After the first cycle's completion, the amount of the metals was quantified by ICP-OES as in the recovered catalyst as in the supernatant solution and it was compared with those measured in the fresh catalyst and in the digestion blank (Figure 9). Noteworthy, no leaching was detected as the metal composition and concentration remained constant in the recovered and fresh catalyst. Moreover the metals abundance in the supernatant was comparable with that of the digestion blank. We performed an accurate characterization of the catalyst after the first cycle using electron microscopy. TEM (Figure 10 and Figure S28) and STEM (Figure S28) images show that recovered $Co_xFe_{3-x}O_4$-DMSA-Au NPs formed aggregates probably included in an amorphous material, justifying the decreased reaction rate observed after the first cycle.[19] Nevertheless, $Co_xFe_{3-x}O_4$-DMSA-Au NPs are not sintered, maintaining their single crystal

nature. By EDX analysis (Figure S29) we calculated the atomic percentage of iron, cobalt and gold (79.1%, 10.1% and 10.4%, respectively; x = 0.34). This result is in agreement with the concentration ratio measured by ICP-OES and, qualitatively, also with the EELS spectrum (Figure S30). Finally, ESI images (Figure S31) confirm the homogeneous distribution of iron and cobalt in the ferrite NPs of the recovered catalyst.

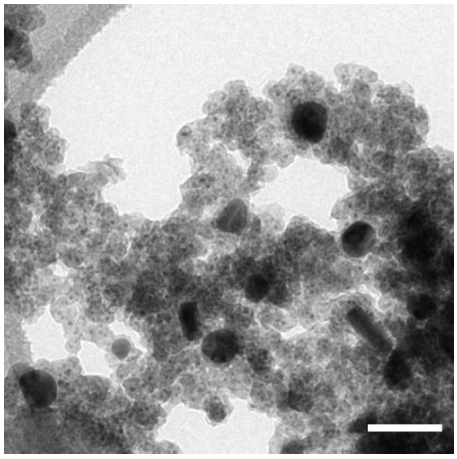

Figure 10. TEM image of the recovered catalyst after one cycle. The bar corresponds to 20 nm.

4. CONCLUSIONS

In this paper we reported an effective synthetic procedure to obtain water dispersible hybrid hetero-structured NPs, composed by a cobalt ferrite nanocore decorated by ultrasmall gold NPs. The designed protocol exploits the presence of 2,3-*meso*-dimercapto succinic acid acting both as coordinate ligand for water colloidal cobalt ferrite and as reducing agent for Au^{3+} ions. Thanks to its versatility, the procedure can be potentially applied to any type of spinel ferrite NPs, $M_xFe_{3-x}O_4$ (M = Fe, Zn, Mn, Cu, Ni). A full characterization of each step has been provided, highlighting the factors that play a crucial role in the decoration step. Moreover, taking advantage of the ultrasmall size of Au NPs, we demonstrated that $Co_xFe_{3-x}O_4$-DMSA-Au NPs acted as efficient catalyst for the reduction of 4-NP to 4-AP showing a full conversion down to

2% molar of catalyst with an excellent k_{norm} = $4.4 \cdot 10^6 s^{-1} mol^{-1}$. Finally, by exploiting the magnetization of cobalt ferrite NPs, the catalyst was magnetically recovered and recycled up to 5 times, maintaining a very high k_{obs} over the cycles.

ASSOCIATED CONTENT

Supporting Information. Synthesis of $Co_xFe_{3-x}O_4$-OA NPs. Figure S1: TEM and statistical distribution. Figure S2: HRTEM and diffraction pattern. Figure S3: EDX Spectrum. Ligand exchange procedure ($Co_xFe_{3-x}O_4$-DMSA NPs). Figure S4: picture of NPs before and after ligand exchange. Figure S5: TEM images of $Co_xFe_{3-x}O_4$-OA NPs and $Co_xFe_{3-x}O_4$-DMSA NPs. Figure S6: statistical distribution. Figure S7: DLS size distribution of $Co_xFe_{3-x}O_4$-OA NPs and $Co_xFe_{3-x}O_4$-DMSA NPs. Figure S8: variation of the ζ-potential in function of pH and ionic strength. Figure S9: FTIR spectra. Figure S10: ICP-OES analysis. Synthesis of $Co_xFe_{3-x}O_4$-DMSA-Au NPs. Figure S11: optimization process. Figure S12: STEM image of $Co_xFe_{3-x}O_4$-DMSA-Au NPs obtained by single injection. Figure S13: statistical size distribution of Au NPs. Figure S14: multimodal size distribution and ζ-potential value. Figure S15: STEM images of $Co_xFe_{3-x}O_4$-DMSA-Au NPs. Figure S16: diffraction pattern. Figure S17: ICP-OES. Figure S18: EDX Spectrum. Magnetic properties of cobalt ferrite NPs. Figure S19: ZFC and FC magnetization of $Co_xFe_{3-x}O_4$-DMSA NPs. Figure S20: ZFC and FC magnetization of $Co_xFe_{3-x}O_4$-DMSA-Au NPs. Catalytic activity of $Co_xFe_{3-x}O_4$-DMSA-Au NPs. Figure S21. Schematic representation of LH model. Figure S22: reduction efficiency after incubation with $NaBH_4$. Figure S23: reduction efficiency after incubation with 4-NP. Table S24: k_{obs} and k_{norm}. Figure S25: TEM images of Au-DMSA NPs before and after catalytic reaction. Figure S26: UV-vis spectrum of Au-DMSA NPs.

Figure S27: picture of the recovering of catalyst. Figure S28: TEM and STEM of $Co_xFe_{3-x}O_4$-DMSA-Au NPs after 1st cycle. Figure S29: EDX of $Co_xFe_{3-x}O_4$-DMSA-Au NPs after 1st cycle. Figure S30: EELS of $Co_xFe_{3-x}O_4$-DMSA-Au NPs after 1st cycle. Figure S31: TEM and EFTM of $Co_xFe_{3-x}O_4$-DMSA-Au NPs after 1st cycle. This material is available free of charge via the Internet at http://pubs.acs.org.

AUTHOR INFORMATION

Corresponding Author

*E-mails: laura.polito@istm.cnr.it; anna.ferretti@istm.cnr.it

Notes

The authors declare no competing financial interest.

Author Contributions

The manuscript was written through contributions of all authors. All authors have given approval to the final version of the manuscript.

ACKNOWLEDGMENT

This work has been financially supported by Regione Lombardia (Italy) through the project RSPPTECH. LP thanks MIUR (Italy) for (PRIN 2010-2011: contract 2010JMAZML_003).

REFERENCES

(1) Song, H. Metal hybrid nanoparticles for catalytic organic and photochemical transformations. *Acc. Chem. Res.* **2015**, 48, 491−499.

(2) Sankar, M.; Dimitratos, N.; Miedziak, P.J.; Wells, P.P.; Kielye, C.J.;Hutchings, G.J. Designing bimetallic catalysts for a green and sustainable future. *Chem. Soc. Rev.* **2012**, 41, 8099–8139.

(3) Wu, X.; Gao, Y.; Dong, C.-M. Polymer/gold hybrid nanoparticles: from synthesis to cancer theranostic applications. *RSC Adv.* **2015**, 5, 13787-13795.

(4) Banin, U.; Ben-Shahar, Y.; Vinokurov, K. Hybrid semiconductor−metal nanoparticles: from architecture to function. *Chem. Mater.* **2014**, 26, 97−110.

(5) Wang, D. Li, Y. Bimetallic nanocrystals: liquid-phase synthesis and catalytic applications. *Adv. Mater.* **2011**, 23, 1044–1060.

(6) Carbone, L.; Cozzoli, P. D. Colloidal heterostructured nanocrystals: Synthesis and growth mechanisms. *Nano Today* **2010**, 5, 449–493.

(7) Leung, K.C.-F.; Xuan, S.; Zhu, X.; Wang, D.; Chak, C.-P.; Lee, S.-F.; Hob, W.K.-W.; Chung B.C.-T. Gold and iron oxide hybrid nanocomposite materials. *Chem. Soc. Rev.* **2012**, 41, 1911–1928.

(8) Goon, I.Y.; Lai, L.M.H.; Lim, M.; Munroe, P.; Gooding, J.J. Amal, R. Fabrication and dispersion of gold-shell-protected magnetite nanoparticles: systematic control using polyethyleneimine. *Chem. Mater.* **2009**, 21, 673–681.

(9) Park, H.-Y.; Schadt, M.J.; Wang, L.; Lim, I-I. S.; Njoki, P.N.; Kim, S. H.; Jang, M.-Y.; Luo, J.; Zhong, C.-J. Fabrication of magnetic core@shell Fe oxide@Au nanoparticles for interfacial bioactivity and bio-separation. *Langmuir* **2007**, 23, 9050-9056.

(10) Lyon, J.L.; Fleming, D.A.; Stone, M.B.; Schiffer, P.; Williams, M.E. Synthesis of Fe oxide core/Au shell nanoparticles by iterative hydroxylamine seeding. *Nano Lett.* **2004**, 4, 719-723.

(11) Tintoré, M.; Mazzini, S.; Polito, L.; Marelli, M.; Latorre, A.; Somoza, Á.; Aviñó, A.; Fàbrega, C.; Eritja, R. Gold-coated superparamagnetic nanoparticles for single methyl discrimination in DNA aptamers. *Int. J. Mol. Sci.* **2015**, 16, 27625–27639.

(12) Pineider, F.; de Julià n Fernàndez, C.; Videtta, V.; Carlino, E.; al Hourani, A.; Wilhelm, F.; Rogalev, A.; Cozzoli, P. D.; Ghigna, P.; Sangregorio, C. Spin-Polarization transfer in colloidal magnetic-plasmonic Au/iron oxide hetero-nanocrystals. *ACS Nano* **2013**, 7, 857–866.

(13) Wang, C.; Yin, H.; Dai, S.; Sun, S. A general approach to noble metal-metal oxide dumbbell nanoparticles and their catalytic application for CO oxidation. *Chem. Mater.* **2010**, 22, 3277–3282.

(14) Xu, C.; Xie, J.; Ho, D.; Wang, C.; Kohler, N.; Walsh, E.G.; Morgan, J.R.; Chin, Y.E.; Sun, S. Au–Fe_3O_4 dumbbell nanoparticles as dual-functional probes. *Angew. Chem. Int. Ed.* **2008**, 47, 173 –176.

(15) Yu, H.; Chen, M.; Rice, P.M.; Wang, S.X.; White, R.L.; Sun, S. Dumbbell-like bifunctional Au-Fe_3O_4 nanoparticles. *Nano Lett.* **2005**, 5, 379-382.

(16) Fratila, R.M.; Mitchell, S.G.; del Pino, P.; Grazu, V.; de la Fuente, J.M. Strategies for the biofunctionalization of gold and iron oxide nanoparticles. *Langmuir* **2014**, 30, 15057−15071.

(17) Bagga, K.; Brougham, D.F.; Keyesde, T.E.; Brabazon, D. Magnetic and noble metal nanocomposites for peparation and optical detection of biological species. *Phys. Chem. Chem. Phys.***2015**, 17, 27968-27980.

(18) Wang, D.; Astruc, D. Fast-growing field of magnetically recyclable nanocatalysts. *Chem. Rev.* **2014**, 114, 6949−6985.

(19) Walker, J.M.; Zaleski, J.M. A simple route to diverse noble metal-decorated iron oxide nanoparticles for catalysis. *Nanoscale* **2016**, 8, 1535–1544.

(20) Yang, X.; Yang, M.; Pang, B.; Vara, M.; Xia, Y. Gold Nanomaterials at Work in Biomedicine. *Chem. Rev.* **2015**, 115, 10410−10488.

(21) Taketoshi, A.; Haruta, M. Size- and structure-specificity in catalysis by Gold Clusters. *Chem. Lett.* **2014**, 43, 380–387.

(22) Haruta, M.; Kobayashi, T.; Sano, H.; Yamada, N. Novel gold catalysts for the oxidation of carbon monoxide at a temperature far below 0° C. *Chem. Lett.* **1987**, 405–408.

(23) Limaye, M.V.; Singh, S.B.; Date, S.K.; Kothari, D.; Reddy, V.R.; Gupta, A.; Sathe, V.; Choudhary, R.J.; Kulkarni, S.K. High coercivity of oleic acid capped $CoFe_2O_4$ nanoparticles at room temperature. *J. Phys. Chem. B* **2009**, 113, 9070–9076.

(24) Munjal, S.; Khare, N.; Nehate, C.; Koul, V. Water dispersible $CoFe_2O_4$ nanoparticles with improved colloidal stability for biomedical applications. *J. Magn. Magn. Mater.* **2016**, 404, 166–169.

(25) Mikalauskaitė, A.; Kondrotas, R.; Niaura, G.; Jagminas, A.Gold-Coated Cobalt Ferrite Nanoparticles via Methionine-Induced Reduction. *J. Phys. Chem. C* **2015**, 119, 17398−17407.

(26) Carlà, F.; G.; Campo, Sangregorio, C.; Caneschi, A.; de Juliàn Fernàndez, C.; Cabrera, L.I. Electrochemical characterization of core@shell $CoFe_2O_4$/Au composite. *J. Nanopart Res.* **2013**, 15, 1813-1829.

(27) Pita, M.; Abad, J.M.; Vaz-Dominguez, C.; Briones, C.; Mateo-Martí, E.; Martín-Gago, J.A.; del Puerto Morales, M.; Fernández, V.M. Synthesis of cobalt ferrite core/metallic shell nanoparticles for the development of a specific PNA/DNA biosensor. *J. Colloid Interface Sci.* **2008**, 321, 484–492.

(28) Gallo, J.; Garcia, I.; Padro, D.; Arnaiz, B.; Penades, S. Water-soluble magnetic glyconanoparticles based on metal-doped ferrites coated with gold: Synthesis and characterization. *J. Mater. Chem.* **2010**, 20, 10010–10020.

(29) Zhao, P.; Feng, X.; Huang, D.; Yang, G.; Astrucc, D. Basic concepts and recent advances in nitrophenol reduction by gold- and other transition metal nanoparticles. *Coord. Chem. Rev.* **2015**, 287, 114–136.

(30) Hu, H.; Xin, J.H.; Hu, H.; Wang, X.; Miao, D.; Liu, Y. Synthesis and stabilization of metal nanocatalysts for reduction reactions – a review. *J. Mater. Chem. A* **2015**, 3, 11157-11182.

(31) Zhu, H.; Zhang, S.; Huang, Y.-X.; Wu, L.; Sun, S. Monodisperse $M_xFe_{3-x}O_4$ (M = Fe, Cu, Co, Mn) nanoparticles and their electrocatalysis for oxygen reduction reaction. *Nano Letters* **2013**, 13, 2947-2951.

(32) Negishi, Y.; Tsukuda, T. One-pot preparation of subnanometer-sized gold clusters via reduction and stabilization by meso-2,3-dimercaptosuccinic acid. *J.Am.Chem.Soc.* **2003**, 125, 4046-4047.

(33) Mondini, S.; Ferretti, A.M.; Puglisi, A.; Ponti, A. PEBBLES and PEBBLEJUGGLER: software for accurate, unbiased, and fast measurement and analysis of nanoparticle morphology from transmission electron microscopy (TEM) micrographs. *Nanoscale* **2012**, 4, 5356-5372. Software freely available from the http://pebbles.istm.cnr.it.

(34) Moya, C.; del Puerto Morales, M.; Batlle, X.; Labarta, A. Tuning the magnetic properties of Co-ferrite nanoparticles through the 1,2 hexadecanediol concentration in the reaction mixture. *Phys. Chem. Chem. Phys.* **2015**,17, 13143-13149.

(35) Verbeeck, J.; Van Aert, S. Model based quantification of EELS spectra. *Ultramicroscopy* **2004**, 101, 207–224.

(36) Miguel-Sancho, N.; Bomatí-Miguel, O.; Colom, G.; Salvador, J.-P.; Marco, M.-P.; Santamaría, J. Development of stable, water-dispersible, and biofunctionalizable superparamagnetic iron oxide nanoparticles. *Chem. Mater.* **2011**, 23, 2795–2802.

(37) Palma, S.I.C.J.; Marciell, M.; Carvalho, A.; Veintemillas-Verdaguer, S.; del Puerto Morales, M.; Roque, A.C.A. Effects of phase transfer ligands on monodisperse iron oxide magnetic nanoparticles. *J. Colloid Interface Sci.* **2015**, 437, 147–155.

(38) Irigoyen, J.; Arekalyan, V.B.; Navoyan, Z.; Iturri, J.; Moya, S.E.; Donath, E. Spherical polyelectrolyte brushes' constant zeta potential with varying ionic strength: an electrophoretic study using a hairy layer approach. *Soft Matter* **2013**, 9, 11609-11617.

(39) Chen, Z.P.; Zhang, Y.; Zhang, S.; Xia, J.G.; Liu, J.W.; Xu, K.; Gu, N. Preparation and characterization of water-soluble monodisperse magnetic iron oxide nanoparticles via surface double-exchange with DMSA. *Colloid. Surface A* **2008**, 316, 210-216.

(40) Odio, O.F.; Lartundo-Rojas, L.; Santiago-Jacinto, P.; Martínez, R.; Reguera, E. Sorption of gold by naked and thiol-capped magnetite nanoparticles: an XPS approach. *J. Phys. Chem. C* **2014**, 118, 2776–2791.

(41) Hostetler, M.J.; Wingate, J.E.; Zhong, C.-J.; Harris, J.E.; Vachet, R.W.; Clark, M.R.; Londono, J.D.; Green, S.J.; Stokes, J.J.; Wignall, G.D.; Glish, G.L.; Porter, M.D.; Evans, N.D.; Murray, R.W. Alkanethiolate Gold Cluster Molecules with Core Diameters from 1.5 to 5.2 nm: Core and Monolayer Properties as a Function of Core Size. *Langmuir* **1998**, 14, 17-30.

(42) Malola, S.; Lehtovaara, L.; Enkovaara, J.; Hakkinen, H. Birth of the localized surface plasmon resonance in monolayer-protected gold nanoclusters. *ACS Nano* **2013**, 7, 10263–10270.

(43) Manova, E.; Kunev, B.; Paneva, D.; Mitov, I.; Petrov, L.; Estournès, C.; D'Orlèans, C.; Rehspringer, J.L.; Kurmoo, M. Mechano-Synthesis, Characterization, and Magnetic Properties of Nanoparticles of Cobalt Ferrite, $CoFe_2O_4$. *Chem .Mat.* **2004**,16,5689-

(44) Li, D.; Diroll, Doan-nguyen, T.V.V.T.; Kikkawa, J.M.; Murray, C.B. Synthesis and Size-Selective Precipitation of Monodisperse Nonstoichiometric $M_xFe_{3-x}O_4$ (M=Mn, Co) Nanocrystals and Their DC and AC Magnetic Properties. *Chem. Mater.* **2016**, 28, 480−489.

(45) Peddis, D.; Cannas, C.; Piccaluga, G.; Agostinelli, E.; Fiorani, D. Spin-glass-like freezing and enhanced magnetization in ultra small $CoFe_2O_4$ nanoparticles. *Nanotechnology*, **2010**,21,125705-

(46) Usov, N.A.; Peschany, S.E. Theoretical hysteresis loops for single-domain particles with cubic anisotropy. *J.Magn.Magn.Mater.* **1997**, 174, 247-260.

(47) Walkert, M.; Mayof, P.I.; O'Gradyt, K.; Charlest, S.W.; Chantrell, R.W. The magnetic properties of single-domain particles with cubic anisotropy: I. Hysteresis loops. *J. Phys: Condens. Matter* **1993**, 5, 2779-2792.

(48) Della Pina, C.; Ferretti, A.M.; Ponti, A.; Falletta, E. A green approach to magnetically-hard electrically –conducting polyaniline/$CoFe_2O_4$ nanocomposites. *Composites Science and technology* **2015**, 110,138-144.

(49) Coey, J.M.D. in Magnetism and magnetic materials. Cambridge university press 2009.

(50) Del Bianco, L.; Hernando A, Fiorani D in Surface Effects in Magnetic Nanoparticles, ed. Fiorani D., Springer, New York. 217-238.

(51) Singh, C.; Goyal, A.; Singhal, S. Nickel-doped cobalt ferrite nanoparticles: efficient catalysts for the reduction of nitroaromatic compounds and photo-oxidative degradation of toxic dyes. *Nanoscale*, **2014**, 6, 7959-7970.

(52) Wunder, S.; Polzer, F.; Lu, Y.; Mei, Y.; Ballauff, M. Kinetic analysis of catalytic reduction of 4-nitrophenol by metallic nanoparticles immobilized in spherical polyelectrolyte brushes. *J. Phys. Chem. C* **2010**, 114, 8814–8820.

(53) Cao, J.; Mei, S.; Ott, A.; Ballauff, M.; Lu, Y. In situ synthesis of catalytic active Au nanoparticles onto gibbsite-polydopamine core-shell nanoplates. *Langmuir* **2015**, 31, 9483–9491.

(54) Lin, F.; Doong, R. Hygly efficient reduction of 4-nitrophenol by heterostructured gold-magnetite nanocatalysts. *Appl. Catal. A-Gen.* **2014**, 486, 32-41.

(55) Lee, Y.; Garcia, M.A.; Huls, N.A.F.; Sun, S. Synthetic tuning of the catalytic properties of Au-Fe_3O_4 nanoparticles. *Angew. Chem. Int. Ed.* **2010**, 49, 1271 –1274.

(56) Pei, F.; Wang, Y.; Wanga, X.; He, P.; Chen, Q.; Wang, X.; Wang, H.; Yi, L.; Guo, J. Performance of supported Au–Co alloy as the anode catalyst of direct borohydride-hydrogen peroxide fuel cell. *Int.J.Hydrogen Energ.* **2010**, 35, 8136-8142.

(57) Goyal, A.; Bansal S.; Kumar, V.; Singh, J.; Singhal, S. Mn substituted cobalt ferrites ($CoMn_xFe_{2-x}O_4$(x = 0.0, 0.2, 0.4, 0.6, 0.8,1.0)): As magnetically separable heterogeneous nanocatalyst for the reduction of nitrophenols. *Applied Surface Science* **2015**, 324, 877–889.

Insert Table of Contents Graphic and Synopsis Here